3104 *Inorg. Chem.* **2010**, *49*, 3104–3112
DOI: 10.1021/ic901733h

Inorganic Chemistry
Article

Spectroscopic and Computational Studies of a *trans*-μ-1,2-Disulfido-Bridged Dinickel Species, $[\{(tmc)Ni\}_2(S_2)](OTf)_2$: Comparison of End-on Disulfido and Peroxo Bonding in $(Ni^{II})_2$ and $(Cu^{II})_2$ Species

Katherine M. Van Heuvelen,[†] Matthew T. Kieber-Emmons,[‡,§] Charles G. Riordan,[‡] and Thomas C. Brunold*[,†]

[†]*Department of Chemistry, University of Wisconsin—Madison, Madison, Wisconsin 53706, and* [‡]*Department of Chemistry and Biochemistry, University of Delaware, Newark, Delaware 19716.* [§]*Present address: Department of Chemistry, Stanford University, Stanford, California 94305*

Received August 31, 2009

A powerful means of enhancing our understanding of the structures and functions of enzymes that contain nickel−sulfur bonds, such as Ni superoxide dismutase, acetyl-coenzyme A synthase/carbon monoxide dehydrogenase, [NiFe] hydrogenase, and methyl-CoM reductase, involves the investigation of model compounds with similar structural and/or electronic properties. In this study, we have characterized a *trans*-μ-1,2-disulfido-bridged dinickel(II) species, $[\{(tmc)Ni\}_2(S_2)]^{2+}$ (**1**, tmc = 1,4,8,11-tetramethyl-1,4,8,11-tetraazacyclotetradecane) by using electronic absorption, magnetic circular dichroism (MCD), and resonance Raman (rR) spectroscopic techniques, as well as density functional theory (DFT) and time-dependent DFT computational methods. Our computational results, validated on the basis of the experimental MCD data and previously reported ^{1}H NMR spectra, reveal that **1** is best described as containing two antiferromagnetically coupled high-spin Ni^{II} centers. A normal coordinate analysis of the rR vibrational data was performed to quantify the core bond strengths, yielding force constants of k_{Ni-S} = 2.69 mdyn/Å and k_{S-S} = 2.40 mdyn/Å. These values provide a useful basis for a comparison of metal−S/O bonding in **1** and related $Ni_2(O_2)$, $Cu_2(O_2)$, and $Cu_2(S_2)$ dimers. In both the disulfido and the peroxo species, the lower effective nuclear charge of Ni^{II} as compared to Cu^{II} results in a decreased covalency, and thus relatively weaker metal−S/O bonding interactions in the Ni_2 dimers than in the Cu_2 complexes.

I. Introduction

Studies of redox-active Ni-dependent enzymes, such as Ni superoxide dismutase,[1] acetyl-coenzyme A synthase/carbon monoxide dehydrogenase (ACS/CODH),[2,3] [NiFe] hydrogenase,[4] and methyl-coenzyme M reductase (MCR),[5] have greatly benefited from parallel investigations of synthetic compounds that mimic the active-site structures and/or reactivities of these enzymes. For example, the Ni^{II} species *RRSS*-[(tmc)Ni](OTf) (tmc = 1,4,8,11-tetramethyl-1,4,8,11-tetraazacyclotetradecane; OTf = $CF_3SO_3^-$) serves as a model of the Ni-containing cofactor of MCR, named F_{430} for its characteristic absorption band at ∼430 nm.[5] Like the hydrocorphin macrocycle of F_{430}, the tmc ligand can support multiple Ni oxidation states, thus mimicking the redox properties of the native cofactor (i.e., both Ni^{I} and Ni^{II} forms of this complex can be isolated). Additionally, [(tmc)Ni](OTf) reacts readily with organic disulfides of the form RSSR′, which are similar to, albeit more reactive than, the MCR substrate $CH_3-S-CoM$ (CoM = $(CH_2)_2SO_3^-$). The products formed in these reactions, such as $[(tmc)Ni(SC_6H_5)](OTf)$, are five-coordinate and contain high-spin Ni^{II} centers.[6] The versatility of the tmc ligand also led to its use in the synthesis of models of ACS/CODH.[7] For example, studies of the electronic structure of the five-coordinate complex $[(tmc)NiCH_3]OTf$ have been carried out to evaluate the nature of the putative $Ni-CH_3$ intermediate in the catalytic cycle of the A-cluster of ACS/CODH.[8]

[(tmc)Ni](OTf) has also been used to explore the reactivity of a Ni^{I} complex with dioxygen. Because of its tetradentate

*To whom correspondence should be addressed. E-mail: brunold@chem.wisc.edu.

(1) Fiedler, A. T.; Bryngelson, P. A.; Maroney, M. J.; Brunold, T. C. *J. Am. Chem. Soc.* **2005**, *127*, 5449–5462.
(2) Ragsdale, S. W.; Kumar, M. *Chem. Rev.* **1996**, *96*, 2515–2539.
(3) Brunold, T. C. *J. Biol. Inorg. Chem.* **2004**, *9*, 533–541.
(4) Volbeda, A.; Charon, M.-H.; Piras, C.; Hatchikian, E. C.; Frey, M.; Fontecilla-Camps, J. C. *Nature* **1995**, *373*, 580–587.
(5) Ermler, U.; Grabarse, W.; Shima, S.; Goubeaud, M.; Thauer, R. K. *Science* **1997**, *278*, 1457–1462.
(6) Ram, M. S.; Riordan, C. G.; Ostrander, R.; Rheingold, A. L. *Inorg. Chem.* **1995**, *34*, 5884–5892.
(7) Ram, M. S.; Riordan, C. G.; Yap, G. P. A.; LiableSands, L.; Rheingold, A. L.; Marchaj, A.; Norton, J. R. *J. Am. Chem. Soc.* **1997**, *119*, 1648–1655.
(8) Schenker, R.; Mock, M. T.; Kieber-Emmons, M. T.; Riordan, C. G.; Brunold, T. C. *Inorg. Chem.* **2005**, *44*, 3605–3617.

Published on Web 03/03/2010
© 2010 American Chemical Society

Scheme 1

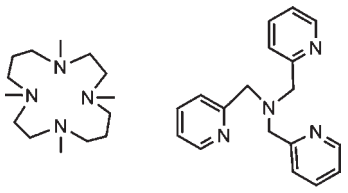

nature and steric bulk, the tmc ligand was found to favor the formation of the "end-on" *trans*-μ-1,2-O_2 $(Ni^{II})_2$ core over the "side-on" μ-η^2:η^2-O_2 $(Ni^{II})_2$ configuration.[9] In a recent study, we compared this $Ni_2(O_2)$ species, $[\{(tmc)Ni\}_2(O_2)]^{2+}$ (**2**), to $[\{(TMPA)Cu\}_2(O_2)]^{2+}$ (TMPA = tris-(2-pyridylmethyl)amine), both of which possess a *trans*-μ-1,2-O_2 $(M^{II})_2$ core structure.[10] It was found that the M−O and O−O bonds are weaker in the dinickel species than in the dicopper complex by 26% and 16%, respectively (for **2**, k_{Ni-O} = 1.52 mdyn/Å and k_{O-O} = 2.58 mdyn/Å). This difference was attributed to the lower effective nuclear charge of Ni^{II} as compared to Cu^{II}, which leads to an increased energy separation of the Ni^{II} 3d orbitals from the frontier orbitals of the O_2 moiety and, thus, to a weakened M−O bonding interaction. The effects of the different supporting ligands (tmc versus TMPA (Scheme 1) for the Ni and Cu species, respectively) and small variations in the M−O−O bond angle were also considered but were found to be minor contributors to the differences in M−O and O−O bond strengths.[10]

The influence of the bridging ligand on the electronic structures of Cu_2 dimers has also been investigated, using $[\{(TMPA)Cu\}_2(trans\text{-}1,2\text{-}\mu\text{-}L_2)]^{2+}$ (L = O, S) as an example.[11] The electronic absorption (Abs) spectrum of each of these species is dominated by an intense L_2 (π^*_σ) → Cu charge transfer transition, which occurs at ~19,000 and 17,600 cm^{-1} in the peroxo and disulfido species, respectively.[11,12] Resonance Raman (rR) spectroscopic studies of these species yielded S−S and Cu−S stretching frequencies of ν_{S-S} = 499 cm^{-1} and ν_{Cu-S} = 316 cm^{-1}, respectively. A quantitative interpretation of these data within the framework of a normal coordinate analysis (NCA) revealed that the S−S bond is 23% weaker than the O−O bond in the peroxo counterpart (k_{S-S} = 2.41 mdyn/Å versus k_{O-O} = 3.11 mdyn/Å), while the Cu−S bond is 32% stronger than the Cu−O bond (k_{Cu-S} = 2.88 mdyn/Å versus k_{Cu-O} = 2.02 mdyn/Å). Computational studies led to the suggestion that these differences reflect the increased covalency of the Cu−S bonds relative to the Cu−O bonds.[11,13] rR studies of a related disulfido species, $[\{(TMPA')Cu\}_2(trans\text{-}1,2\text{-}\mu\text{-}S_2)]^{2+}$, in which the TMPA ligand was modified by the addition of a 6-CH_2OCH_3 group to one pyridyl ligand arm so as to obtain a spectroscopically pure sample, yielded similar results, that is, ν_{S-S} = 492 cm^{-1} and ν_{Cu-S} = 309 cm^{-1}.[14]

To expand these studies of peroxo and disulfido dinickel and dicopper species, we have investigated the spectral and electronic properties of a disulfido $(Ni^{II})_2$ complex, $[\{(tmc)Ni\}_2(S_2)](OTf)_2$ (**1**), by using a combined spectroscopic and computational approach. While a small number of nickel−sulfur species have been studied in the past,[15−25] we present here a detailed characterization of the electronic structure of the first *trans*-μ-1,2-S_2 (Ni^{II}_2) core. The Abs, magnetic circular dichroism (MCD), and rR spectroscopic data of **1** are analyzed within the framework of density functional theory (DFT) and time-dependent DFT (TD-DFT) computations. Collectively, the results obtained in this study provide significant new insight into how the identity of the metal ions, as well as the bridging and supporting ligands, influence the electronic structures of dinickel and dicopper complexes.

II. Experimental Section

II.A. Spectroscopy. Samples of **1** suitable for spectroscopic studies were prepared according to previous reports.[26] Maximal yields of **1** were obtained by the dropwise addition of a concentrated sulfur solution to a dilute [(tmc)Ni](OTf) solution at low temperature (< 233 K). Tetrahydrofuran (THF) solutions of **1** used for spectroscopic experiments were prepared with a concentration of 5 mg/11.25 mL THF. Low-temperature Abs and MCD spectra were obtained using a Jasco J-715 spectropolarimeter in conjunction with an Oxford Instruments SM-4000 8T magnetocryostat. For all MCD data, the −7 T spectrum was subtracted from the +7 T spectrum to eliminate contributions from glass strain.

For rR studies, isotopically pure samples of **1** in THF were prepared in NMR tubes. ^{34}S (99%) was purchased from Trace Scientific, Inc. and purified by double recrystallization from hot toluene under an inert atmosphere. An Ar^+ ion laser (Coherent I-305), a Kr^+ ion laser (Coherent I-302C), and a dye laser (Coherent 599−01, equipped with rhodamine 6G dye) pumped by the Ar^+ laser were used as the excitation sources, keeping the power at the sample in the range of 10−20 mW. Samples were placed in an EPR dewar flask filled with liquid nitrogen to minimize photo-decomposition. The scattered light was collected at a ~135° backscattering angle from the surface of the sample and dispersed by an Acton Research triple monochromator with 1200 or 2400 grooves/mm gratings. Data were collected using a CCD camera (Princeton Instruments Spec X: 100 BR deep depletion, back-thinned, 1340 × 100 pixels). The 880 cm^{-1} peak of the THF solvent was used as the standard for

(9) Kieber-Emmons, M. T.; Schenker, R.; Yap, G. P. A.; Brunold, T. C.; Riordan, C. G. *Angew. Chem., Int. Ed.* **2004**, *43*, 6716–6718.
(10) Schenker, R.; Kieber-Emmons, M. T.; Riordan, C. G.; Brunold, T. C. *Inorg. Chem.* **2005**, *44*, 1752–1762.
(11) Chen, P.; Fujisawa, K.; Helton, M. E.; Karlin, K. D.; Solomon, E. I. *J. Am. Chem. Soc.* **2003**, *125*, 6394–6408.
(12) Baldwin, M. J.; Ross, P. K.; Pate, J. E.; Tyeklar, Z.; Karlin, K. D.; Solomon, E. I. *J. Am. Chem. Soc.* **1991**, *113*, 8671–8679.
(13) Helton, M. E.; Chen, P.; Paul, P. P.; Tyeklar, Z.; Sommer, R. D.; Zakharov, L. N.; Rheingold, A. L.; Solomon, E. I.; Karlin, K. D. *J. Am. Chem. Soc.* **2003**, *125*, 1160–1161.
(14) Maiti, D.; Woertink, J. S.; Vance, M. A.; Milligan, A. E.; Sarjeant, A. A. N.; Solomon, E. I.; Karlin, K. D. *J. Am. Chem. Soc.* **2007**, *129*, 8882–8892.
(15) Cho, J.; Yap, G. P. A.; Riordan, C. G. *Inorg. Chem.* **2007**, *46*, 11308–11315.
(16) Cho, J.; Van Heuvelen, K. M.; Yap, G. P. A.; Brunold, T. C.; Riordan, C. G. *Inorg. Chem.* **2008**, *47*, 3931–3933.
(17) Oster, S. S.; Lachicotte, R. J.; Jones, W. D. *Inorg. Chim. Acta* **2002**, *330*, 118–127.
(18) Pleus, R. J.; Waden, H.; Saak, W.; Haase, D.; Pohl, S. *J. Chem. Soc., Dalton Trans.* **1999**, 2601–2610.
(19) Mealli, C.; Midollini, S.; Sacconi, L. *Inorg. Chem.* **1978**, *17*, 632–637.
(20) Mealli, C.; Midollini, S. *Inorg. Chem.* **1983**, *22*, 2785–2786.
(21) Kruger, T.; Krebs, B.; Henkel, G. *Angew. Chem., Int. Ed. Engl.* **1989**, *28*, 61–62.
(22) Kruger, T.; Krebs, B.; Henkel, G. *Angew. Chem., Int. Ed. Engl.* **1992**, *31*, 54–56.
(23) Tremel, W.; Krebs, B.; Henkel, G. *Inorg. Chim. Acta, Bioinorg. Chem.* **1983**, *80*, L31–L32.
(24) Tremel, W.; Kriege, M.; Krebs, B.; Henkel, G. *Inorg. Chem.* **1988**, *27*, 3886–3895.
(25) Tremel, W.; Henkel, G. *Inorg. Chem.* **1988**, *27*, 3896–3899.
(26) Kieber-Emmons, M. T.; Van Heuvelen, K. M.; Brunold, T. C.; Riordan, C. G. *J. Am. Chem. Soc.* **2009**, *131*, 440–441.

calibrating the frequencies and relative intensities of the rR features of **1**.

II.B. Computations. II.B.1. Geometry Optimizations. The Amsterdam Density Functional (ADF) 2004 suite of programs[27−30] was used to refine the atomic positions of **1**, for which no crystal structure is currently available. Initial coordinates for the model of **1** were derived from its previously characterized peroxo counterpart, **2**.[10] The four methyl groups of each tmc ligand of **1** were replaced with hydrogen atoms for computational practicality. Combined quantum mechanics/molecular mechanics studies revealed this truncation does not significantly affect the computed geometric and electronic properties of **1** (Supporting Information, Table S2). All computations were performed on a cluster of Intel Xeon processors (ACE computers) using ADF basis set IV (a triple-ζ basis set), an integration constant of 4.0, and the Vosko−Wilk−Nusair local density approximation (VWN-LDA)[31] with the nonlocal gradient corrections of Becke for exchange[32] and Perdew for correlation.[33] Core electrons were frozen through 1s for C, N, and O, and through 2p for Ni and S. Both ferromagnetic (high spin [HS], $S = 2$) and antiferromagnetic (broken symmetry [BS], $M_S = 0$) exchange couplings were considered.

II.B.2. Single-Point Calculations. The ORCA 2.6.35 software package developed by Dr. Frank Neese[34] was used to perform single-point DFT calculations for both the HS and BS states of **1**, in each case using the geometry-optimized model obtained for the BS state. Becke's three-parameter hybrid functional for exchange[35,36] and the Lee−Yang−Parr functional for correlation (B3LYP/G)[37] were used with the polarized split valence (SV(P)) basis[38] and the SV/C auxiliary basis[39] for all atoms except Ni, for which Ahlrichs' polarized triple-ζ valence polarization (TZVP) basis[40] was used instead. All computations were performed spin unrestricted and with an integration grid of size 4 (302 Lebedev points). The BrokenSym keyword was employed to obtain the antiferromagnetically coupled BS ground-state wave function.

II.B.3. TD-DFT Calculations. TD-DFT calculations were also performed with the ORCA 2.6.35 software package,[34] using the same basis sets and parameters as specified above for the single-point calculations. To permit a direct comparison with our experimental data, the TD-DFT results were used to simulate Abs spectra by assuming that each electronic transition gives rise to a Gaussian band with a full width at half-maximum of $\nu_{1/2} = 2{,}900\ \mathrm{cm}^{-1}$. The natures of key electronic transitions were explored on the basis of isosurface plots of molecular orbitals (MOs) and electron density difference maps (EDDMs), which were generated with the gOpenMol program developed by Laaksonen[41] using isodensity values of 0.03 au and 0.003 au, respectively.

II.C. NCA. A NCA of the vibrational data of **1** was conducted using the QCPE 576/QCMP 067 program developed by McIntosh and Peterson.[42] To reduce the number of parameters, a C_{2h} idealized geometry of the $Ni_2(S_2)$ core was assumed, which was derived from the DFT-optimized structure of **1** (Figure 5). Moreover, the torsional mode was omitted from the analysis, leaving three symmetry inequivalent internal coordinates: the Ni−S and S−S stretching coordinates and the Ni−S−S bending coordinate. The corresponding force constants, together with four stretch/stretch and stretch/bend interaction constants, were allowed to vary until the calculated frequencies for the ν_{S-S} and ν_{Ni-S} modes and the corresponding $^{32}S \rightarrow {}^{34}S$ isomer shifts properly reproduced the experimental vibrational data. The complete force field and further details about the NCA are provided in Supporting Information, Table S3.

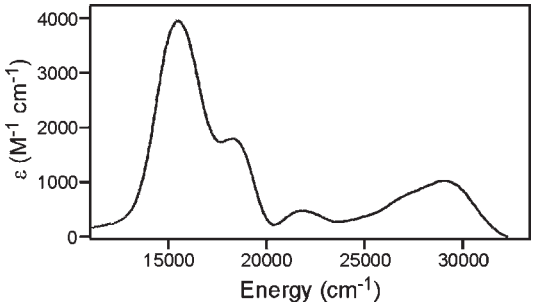

Figure 1. Abs spectrum of **1** in THF at 195 K.

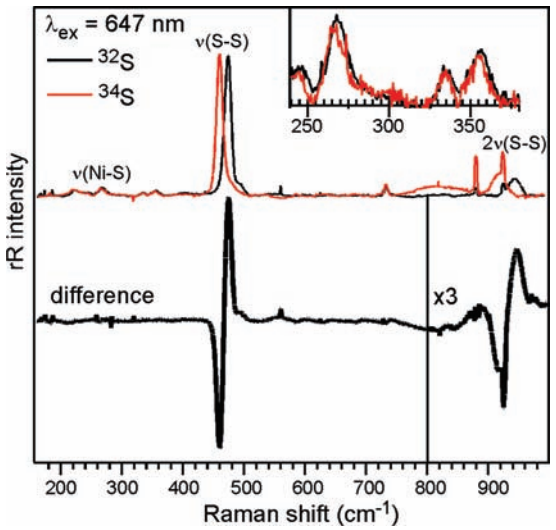

Figure 2. Top: 77 K rR spectra obtained with $\lambda_{ex} = 647$ nm excitation for samples of **1** prepared with ^{32}S (black) and ^{34}S (red). Bottom: Difference spectrum.

II.D. Abs and rR Excitation Profile Data Simulations. The relevant portions of the 4 K Abs spectrum and 77 K rR excitation profiles of **1** were simulated using time-dependent Heller theory[43,44] as implemented in a MathCAD script. A damping factor of $\Gamma = 500\ \mathrm{cm}^{-1}$ was used for both simulations.

III. Results

III.A. Spectroscopy. The Abs spectrum of **1** in THF solution (Figure 1) is dominated by a broad feature at $15{,}500\ \mathrm{cm}^{-1}$ ($\varepsilon \approx 4{,}000\ \mathrm{M}^{-1}\ \mathrm{cm}^{-1}$) that exhibits a shoulder

(27) Baerends, E. J.; Ellis, D. E.; Ros, P. *Chem. Phys.* **1973**, *2*, 41.
(28) Versluis, L.; Ziegler, T. *J. Chem. Phys.* **1988**, *88*, 322–328.
(29) Velde, G. T.; Baerends, E. J. *J. Comput. Phys.* **1992**, *99*, 84–98.
(30) Guerra, C. F.; Snijders, J. G.; te Velde, G.; Baerends, E. J. *Theor. Chem. Acc.* **1998**, *99*, 391–403.
(31) Vosko, S. H.; Wilk, L.; Nusair, M. *Can. J. Phys.* **1980**, *58*, 1200–1211.
(32) Becke, A. D. *J. Chem. Phys.* **1986**, *84*, 4524–4529.
(33) Perdew, J. P. *Phys. Rev. B* **1986**, *33*, 8822–8824.
(34) Neese, F., *ORCA 2.6.35, an ab initio, density functional, and semi-empirical program package*; Max-Planck-Institut für Bioanorganische Chemie: Mülheim an der Ruhr, Germany, 2008.
(35) Becke, A. D. *J. Chem. Phys.* **1993**, *98*, 5648–5652.
(36) Becke, A. D. *J. Chem. Phys.* **1993**, *98*, 1372–1377.
(37) Lee, C. T.; Yang, W. T.; Parr, R. G. *Phys. Rev. B* **1988**, *37*, 785–789.
(38) Schafer, A.; Horn, H.; Ahlrichs, R. *J. Chem. Phys.* **1992**, *97*, 2571–2577.
(39) Weigend, F.; Haser, M. *Theor. Chem. Acc.* **1997**, *97*, 331–340.
(40) Schafer, A.; Huber, C.; Ahlrichs, R. *J. Chem. Phys.* **1994**, *100*, 5829–5835.
(41) Laaksonen, L. *J. Mol. Graphics* **1992**, *10*, 33–34.
(42) McIntosh, D. F.; Peterson, M. R. *QCPE 576/QCMP 067: General Vibrational Analysis System*; University of Toronto: Toronto.
(43) Bailey, S. E.; Cohan, J. S.; Zink, J. I. *J. Phys. Chem. B* **2000**, *104*, 10743–10749.
(44) Kim Shin, K. S.; Zink, J. I. *J. Am. Chem. Soc.* **1990**, *112*, 7148–7157.

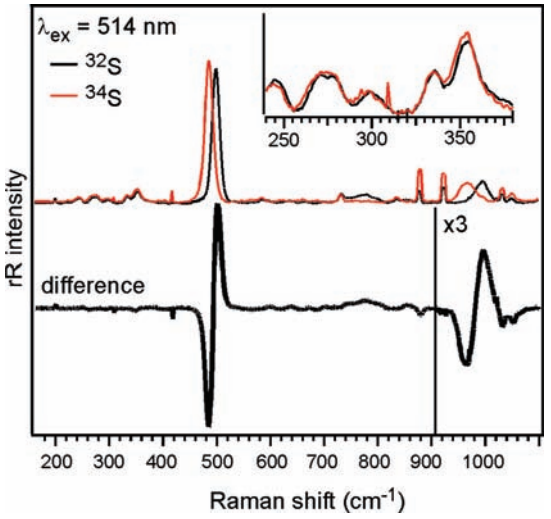

Figure 3. Top: 77 K rR spectra obtained with λ_{ex} = 514 nm excitation for samples of **1** prepared with ^{32}S (black) and ^{34}S (red). Bottom: Difference spectrum.

on its high-energy side at 18,300 cm^{-1} ($\varepsilon \approx$ 1,800 M^{-1} cm^{-1}).[45] By varying the Ni/S ratio during the synthesis of **1**, the relative intensities of these two features were found to change, with the shoulder at 18,300 cm^{-1} gaining intensity at the expense of the 15,500 cm^{-1} band as the molar ratio of S/Ni was increased beyond 1. This finding indicates that the two features arise from distinct species that are present in solution. Similarly, in previous studies of *trans*-μ-1,2-S_2 $(Cu^{II})_2$ dimers, the appearance of multiple overlapping Abs bands was attributed to the formation of several distinct species.[11,14]

To determine which Abs features are associated with **1**, rR studies were performed using multiple laser excitation wavelengths across the visible spectral region. The rR spectrum of **1** obtained using laser excitation of λ_{ex} = 647 nm (15,454 cm^{-1}) to probe the vibrations that couple to the transition responsible for the 15,500 cm^{-1} Abs band exhibits an intense feature at 474 cm^{-1} that shifts to 462 cm^{-1} ($\Delta\nu$ = −12 cm^{-1}) upon $^{32}S \rightarrow {}^{34}S$ isotope substitution (Figure 2). The first overtone of this feature is apparent at 943 cm^{-1} ($\Delta\nu$ = −25 cm^{-1}), while an additional isotopically sensitive band is observed at 269 cm^{-1} ($\Delta\nu$ = −2.5 cm^{-1}). Furthermore, two isotopically insensitive features can be discerned at 335 and 355 cm^{-1}. When the excitation wavelength was moved to λ_{ex} = 514 nm (19,436 cm^{-1}) to enhance the vibrations coupling to the electronic transition associated with the 18,300 cm^{-1} Abs band of the second species, a rR spectrum was obtained that is dominated by a new feature at 501 cm^{-1} (Figure 3). This feature and its associated overtone at 997 cm^{-1} downshift to 488 and 969 cm^{-1}, respectively, upon $^{32}S \rightarrow {}^{34}S$ substitution (Δ = −13 and −28 cm^{-1}, respectively). A second isotopically sensitive feature is observed at 273 cm^{-1} (Δ = −2 cm^{-1}) along with the isotopically insensitive 335 and 355 cm^{-1} features that are also present in the rR spectrum obtained with λ_{ex} = 647 nm (Figure 2).

As shown in Figure 4, the rR excitation profile for the 474 cm^{-1} feature mirrors the 15,500 cm^{-1} Abs band,

(45) Note that the original report of this species reported molar absorptivity per Ni center, not per dimer.

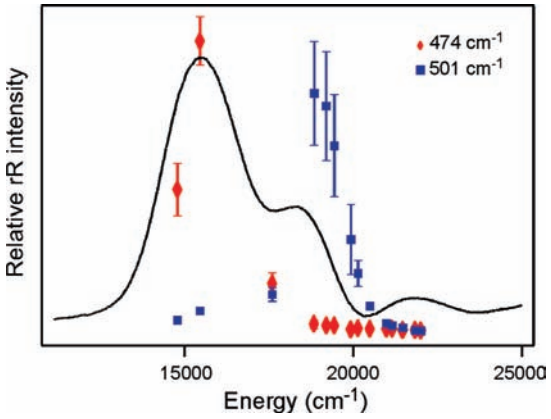

Figure 4. 195 K Abs spectrum of **1** and 77 K rR excitation profiles for the vibrational features at 474 cm^{-1} (red diamonds) and 501 cm^{-1} (blue squares). Error bars correspond to the standard deviation over three data sets.

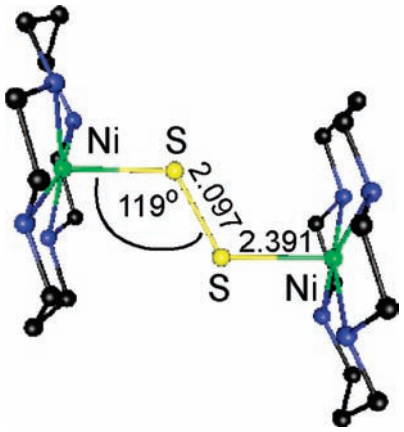

Figure 5. DFT energy-minimized model of **1** obtained using the BS formalism (model $\mathbf{1}^{BS}$).

while that obtained for the 501 cm^{-1} feature traces the higher-energy shoulder at 18,300 cm^{-1}. Alternatively, the rR excitation profiles for the 335 and 355 cm^{-1} features track with both Abs bands (Supporting Information, Figure S1). As these features are in the range expected for Ni−N vibrations, they are tentatively assigned as $\nu_{Ni-N(tmc)}$ vibrational modes. In support of this assignment, rR spectra of **2** exhibit two similar isotopically insensitive features at 336 and 349 cm^{-1} that were also attributed to $\nu_{Ni-N(tmc)}$ vibrations.[10]

To confirm that the 474/269 cm^{-1} and 501/273 cm^{-1} sets of features are due to two distinct species, the following experiment was conducted. After obtaining an initial rR spectrum with λ_{ex} = 647 nm, the sample was irradiated at λ_{ex} = 514 nm using a laser power of up to 200 mW to cause partial photo-decomposition of the species absorbing at this wavelength. As expected, rR spectra collected during this experiment revealed that the 501 and 273 cm^{-1} features decayed in tandem. A final spectrum was then obtained using λ_{ex} = 647 nm, which indicated that the 474 and 269 cm^{-1} features had also diminished in intensity, but to a much lesser extent than the 501/273 cm^{-1} pair that dominate rR spectra obtained with λ_{ex} = 514 nm.

On the basis of the rR data presented above, we assign the 15,500 cm^{-1} Abs band as a disulfido → Ni^{II} charge

Table 1. Experimental and NCA-Predicted Vibrational Frequencies (cm^{-1}) and Potential Energy Distributions (%)

	exp		NCA		potential energy distribution (%)		
mode	^{32}S	^{34}S	^{32}S	^{34}S	Δr_{S-S}	Δr_{Ni-S}	$\Delta\theta_{Ni-S-S}$
A_g ν_{S-S}	474	462	473.6	462.9	64	22	14
B_u ν_{Ni-S}			470.6	461.6	0	100	0
A_g ν_{Ni-S}	269	266.5	270.8	264.4	43	56	1
A_g δ_{Ni-S-S}			144.1	142.5	0	0	100
B_u δ_{Ni-S-S}			78.0	76.5	0	15	85
force constants					k_{S-S} = 2.40 mdyn/Å[a]	k_{Ni-S} = 2.69 mdyn/Å[a]	

[a] See Table 4 for a complete comparison of $M_2(L_2)$ bond strengths.

transfer (CT) transition of **1**, with corresponding vibrational features of ν_{S-S} = 474 cm^{-1} and ν_{Ni-S} = 269 cm^{-1}. The observed $^{32}S \rightarrow {}^{34}S$ isotope shifts of $\Delta = -13$ for ν_{S-S} and $\Delta = -2.5$ cm^{-1} for ν_{Ni-S} are in good agreement with the shifts of -14 and -3 cm^{-1}, respectively, calculated for S−S and Ni−S diatomic harmonic oscillators. These assignments are also consistent with the results from previous rR studies of end-on disulfido $(Cu^{II})_2$ species, for which the ν_{S-S} and ν_{Cu-S} modes were observed within the ranges of 476−499 cm^{-1} and ∼300−400 cm^{-1}, respectively.[1,11,14] The fact that the 501/273 cm^{-1} pair of $^{32}S \rightarrow {}^{34}S$ isotopically sensitive vibrational features that dominate the rR spectrum obtained with λ_{ex} = 514 nm (Figure 3) have similar frequencies as those associated with **1** suggests that the second species that is present in our samples also possesses a $Ni_2(S_2)$ core structure. However, considering that this second species continues to form at higher S/Ni ratios, a $Ni_2(S_3)$ core is a viable alternative. Regardless of these ambiguities, a more detailed characterization of this minority species is beyond the scope of the present study.

Variable temperature MCD studies (data not shown) revealed that **1** is diamagnetic, which is consistent with antiferromagnetic coupling between two high-spin $S = 1$ Ni^{II} centers. The possibility of two low-spin $S = 0$ Ni^{2+} centers can be eliminated on the basis of previously reported ^{1}H NMR data, which revealed paramagnetically shifted resonances diagnostic of moderately strong antiferromagnetic coupling between two high-spin Ni(II) centers.[26] Notably, the low-temperature (4 K) Abs spectrum obtained for the sample used in the MCD experiments (prepared in 2:1 toluene/DMF) shows a single feature in the visible region, at 16,026 cm^{-1} (Supporting Information, Figure S3), in further support of our conclusion that only the 15,500 cm^{-1} band in the 195 K Abs spectrum shown in Figure 1 is associated with **1**.

III.B. NCA. To quantify the Ni−S and S−S bond strengths of **1**, we performed a NCA of the rR data presented in Section III.A.[42] The $Ni_2(S_2)$ core of **1** has a total of 6 vibrational degrees of freedom. Assuming a C_{2h} symmetrized core structure, the corresponding vibrations include three totally symmetric a_g vibrational modes (ν_{S-S}, ν_{Ni-S}, and δ_{Ni-S-S}) and two antisymmetric b_u modes (ν_{Ni-S} and δ_{Ni-S-S}). The sixth mode, mainly involving out-of-plane torsional motion, is expected to contain minimal contributions from the Ni−S and S−S stretching motions and was thus neglected in our analysis.[10,46] The totally symmetric ν_{S-S} and ν_{Ni-S} modes of **1** are observed at 474 and 269 cm^{-1}, respectively (vide supra), while the δ_{Ni-S-S} mode is estimated to lie within the ∼120−140 cm^{-1} range, which is outside of the experimental detection limit.[10,11] As expected on the basis of the selection rules that govern rR band intensities, only the totally symmetric vibrational modes are significantly enhanced and the two b_u vibrational modes are not observed.[47]

The results of the NCA, which was performed as described in Section II.D using a generalized valence force field and the structural parameters provided in Figure 5 and Supporting Information, Table S3, are presented in Table 1. The agreement between the NCA-predicted and experimental frequencies is excellent. The assignment of the 474 cm^{-1} mode as the symmetric ν_{S-S} stretch is confirmed by the potential energy distributions (PEDs) listed in Table 1 (64% S−S, 22% Ni−S). Likewise, the calculated PEDs show that the 269 cm^{-1} mode consists primarily of the symmetric Ni−S vibration (56% Ni−S, 43% S−S). The δ_{Ni-S-S} mode of a_g symmetry is predicted to occur at 144 cm^{-1}, which is within the range of frequencies reported for the δ_{M-L-L} vibrational mode of similar *trans*-μ-1,2-L_2 M_2 species.[10,11] The optimized values for the force constants k_{S-S} and k_{Ni-S} are 2.40 and 2.69 mdyn/Å, respectively, indicating that **1** contains a weaker M−S bond than its $Cu_2(S_2)$ analogue, while the S−S bond strengths in the two species are comparable.[11] The origin of this result is explored in Section IV.

III.C. Computational Studies. III.C.1. Molecular Structure. In computational studies of **1**, we considered both high spin (HS, $S = 2$) and broken symmetry (BS, $M_S = 0$) models. Initial coordinates were derived from **2**, the previously characterized peroxo analogue of **1**.[10] The bridging ligand was changed to a disulfido moiety, and the Ni−S and S−S bond lengths were suitably adjusted based on literature values.[11,48] Both coupling schemes produced similar DFT energy-minimized geometries, with differences in optimized bond lengths of less than 0.05 Å (note that very similar results were obtained in preliminary DFT computations using the Gaussian03 software package,[26] demonstrating that our results are not dependent on the software package or the functional employed). The geometry-optimized model of **1** obtained for the BS state ($\mathbf{1}^{BS}$) is shown in Figure 5. In this structure both Ni centers adopt the square pyramidal geometry previously observed in other transition metal complexes featuring the tmc ligand.[49] Both the core geometry

(46) Brunold, T. C.; Tamura, N.; Kitajima, N.; Moro-oka, Y.; Solomon, E. I. *J. Am. Chem. Soc.* **1998**, *120*, 5674–5690.

(47) Spiro, T. G.; Czernuszewicz, R. S. Resonance Raman Spectroscopy. In *Physical Methods in Bioinorganic Chemistry: Spectroscopy and Magnetism*; Que, L. J., Ed.; University Science Books: Sausalito, CA, 2000.

(48) Bar-Nahum, I.; York, J. T.; Young, V. G., Jr.; Tolman, W. B. *Angew. Chem., Int. Ed.* **2008**, *47*, 533–536.

(49) Micheloni, M.; Paoletti, P.; Burki, S.; Kaden, T. A. *Helv. Chim. Acta* **1982**, *65*, 587–594.

(Ni−L−L bond angles of 119° and 120° for **1** and **2**, respectively) and the coordination of the Ni center by the tmc macrocycle (average Ni−N bond lengths of 2.095 and 2.101 Å in **1** and **2**, respectively) are insignificantly affected by the replacement of the bridging peroxo ligand by a disulfido moiety.[10,50] The calculated S−S bond distance of 2.097 Å is similar to the S−S bond length of 2.051 Å in $[\{(TMPA)Cu\}_2(S_2)]^{2+}$, while the Ni−S bonds are elongated relative to the Cu−S bonds (2.391 and 2.272 Å, respectively).[11]

III.C.2. Exchange Coupling. The total energy of model $\mathbf{1}^{\mathbf{BS}}$ is lower than that of its HS counterpart ($\mathbf{1}^{\mathbf{HS}}$) by 0.54 eV, diagnostic of moderately strong antiferromagnetic coupling between the two Ni^{II} centers. To corroborate this prediction, single-point DFT computations considering ferromagnetic and antiferromagnetic coupling were carried out using the B3LYP hybrid functional. Both calculations used the $\mathbf{1}^{\mathbf{BS}}$ model shown in Figure 5. Here again, the BS state was found to be energetically favored over the HS state, by 0.12 eV. Consequently, our computational results suggest that the two metal centers of **1** are antiferromagnetically coupled to yield a diamagnetic $S = 0$ ground state.

These computational results can also be used to quantitatively assess the strength of the antiferromagnetic exchange interaction in **1**, as expressed in terms of the Heisenberg−Dirac−van Vleck Hamiltonian $\mathbf{H} = -2J\cdot\mathbf{S}_1\cdot\mathbf{S}_2$, where $\mathbf{S_1}$ and $\mathbf{S_2}$ are the spin vectors for Ni centers 1 and 2, respectively. Specifically, by using the energies of the HS and the BS states, E_{HS} and E_{BS}, respectively, the exchange parameter, J, can be calculated as follows:

$$J = \frac{-(E_{HS} - E_{BS})}{(S_{max})^2} \qquad (1)$$

S_{max} refers to the highest possible spin state of the system; hence, $(S_{max})^2 = 4$ for **1**.[51] In this formalism, $J > 0$ corresponds to ferromagnetic coupling, in which case the highest spin state is lowest in energy. Alternatively, when $J < 0$, the lowest spin state is energetically most stable, and the dimer possesses an antiferromagnetically coupled ground state. The calculated value of $J = -240\ cm^{-1}$, obtained using the total energies from the HS and BS B3LYP calculations on the $\mathbf{1}^{\mathbf{BS}}$ model, is indicative of moderately strong antiferromagnetic coupling and consistent with the temperature-independent MCD spectrum of **1** (vide supra).

The calculated J value of $-240\ cm^{-1}$ for **1** is greater in magnitude than $J = -170\ cm^{-1}$ obtained in analogous DFT studies of **2**, suggesting that more efficient superexchange pathways exist in the disulfido dimer than in its peroxo counterpart. This finding is consistent with the greater covalency of the M−L bonds in **1** compared to **2** (see also Section IV.C). In both species, the dominant antiferromagnetic exchange pathway involves the strongly σ-interacting Ni z^2 and L_2 (π^*_σ) orbitals (Figure 6A).[52]

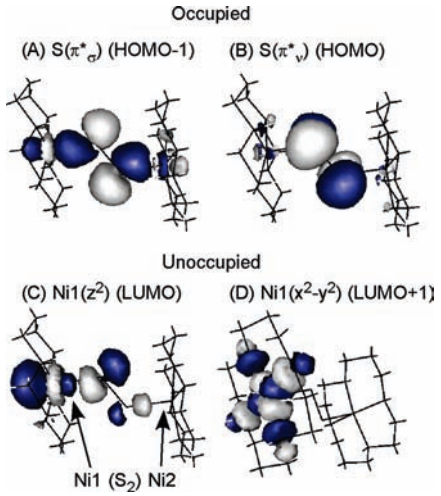

Figure 6. Isosurface plots of key spin-down MOs of the $Ni_2(S_2)$ core of **1**, as obtained from a single-point DFT calculation on model $\mathbf{1}^{\mathbf{BS}}$ using the BS formalism.

Table 2. Energies (in eV) and Compositions (%) of the Ni 3d- and Disulfido-Based Spin-down (β) MOs, as Obtained from a BS DFT Calculation on Model **1a** (see Figure 6 for MO plots)

E (eV)	MO[a]	occ[b]	Ni1	(S_2^{2-})	Ni2	rest
−5.54	Ni 3d (LUMO+1)	0	77 (x^2-y^2)	0	0	23
−7.17	Ni 3d (LUMO)	0	60 (z^2)	15	0	24
−9.32	S_2^{2-} (π^*_ν) (HOMO)	1	2 (yz)	90	1 (yz)	7
−10.24	S_2^{2-} (π^*_σ) (HOMO-1)	1	13 (z^2)	54	3 (z^2)	30

[a] Principal orbital contributor. [b] Occupancy of MO.

III.C.3. Nature of Ni−S and S−S Bonding. To obtain a quantitative bonding description for **1**, spin-unrestricted DFT calculations using the BS approach were performed on the geometry-optimized model $\mathbf{1}^{\mathbf{BS}}$. In the BS approach, **1** is treated as two antiferromagnetically coupled high-spin ($S = 1$) Ni^{II} monomers, causing the spin-up (α) and spin-down (β) electrons to localize on opposite sides of the dimer. As a result, each spin-up molecular orbital (MO) on one side of the dimer has a C_2-symmetric spin-down counterpart of the same energy and composition on the opposite side. The key spin-down MOs of the $Ni_2(S_2)$ core of $\mathbf{1}^{\mathbf{BS}}$ are depicted in Figure 6.

The computed MO descriptions and Ni−L bonding interactions for **1** are strikingly similar to those obtained previously for **2**.[10] The high degree of covalency in **1** is apparent in the significant mixing of disulfido and Ni 3d-orbital character in the occupied disulfido π^*_σ-based orbital and the Ni z^2-based lowest-energy occupied MO (LUMO) depicted in Figure 6. The σ-bonding character of this interaction stabilizes the occupied disulfido π^*_σ orbital relative to its π^*_ν counterpart by 0.92 eV (Table 2), as the latter is perpendicular to the $Ni_2(S_2)$ plane and thus only minimally interacting with the Ni 3d orbitals (Figure 6B).

III.C.4. Excited-State Properties. Both the HS and the BS formalisms were used in TD-DFT calculations on the energy-minimized model $\mathbf{1}^{\mathbf{BS}}$ shown in Figure 5. As both

(50) The BS model contains a Ni−S−S−Ni core that is considerably more planar than that of its HS counterpart (3.3° versus 12.4°, respectively). A similar trend has been noted in a previous study of the Ni peroxo analogue.

(51) Neese, F. *ORCA 2.4.45, an ab initio, density functional, and semi-empirical program package*; Max-Planck-Institut für Bioanorganische Chemie: Mülheim an der Ruhr, Germany, 2005.

(52) In this manuscript, the Ni 3d orbitals are abbreviated (i.e., *xy* for Ni d_{xy}).

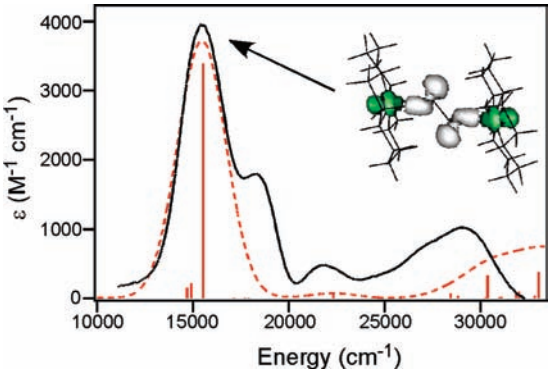

Figure 7. TD-DFT-predicted (dashed line) and experimental (solid line) Abs spectra of **1**. The computed spectrum, obtained for model $\mathbf{1}^{\mathbf{BS}}$, was red-shifted and scaled to facilitate the comparison with the experimental spectrum. Inset: Electron density difference map for the dominant transition (gray and green indicate loss and gain of electron density, respectively).

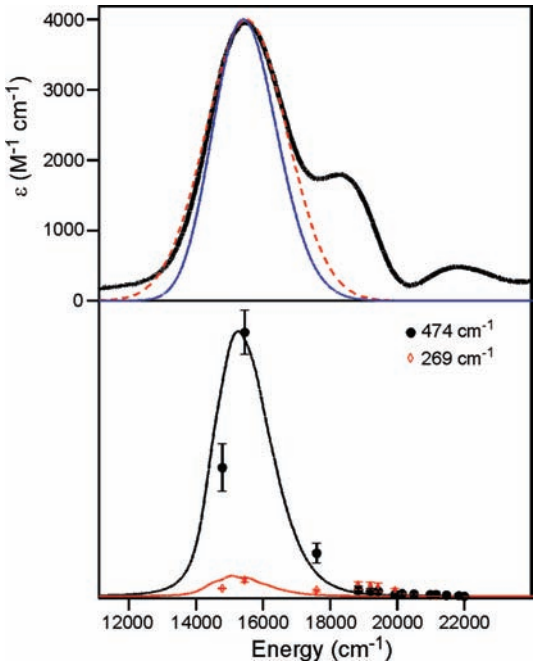

Figure 8. Top: Experimental 4 K Abs spectrum of **1** (thick solid line), Gaussian band used to simulate the dominant Abs feature (dashed line), and TD Heller simulated Abs band (thin solid line) obtained using the parameters listed in Table 3. Bottom: Corresponding experimental rR excitation profiles for the 474 and 269 cm^{-1} modes (black circles and red diamonds, respectively) along with the simulated rR excitation profiles (black and red solid lines, respectively).

formalisms yielded similar TD-DFT computed Abs spectra, only the results obtained from the BS calculation are considered here.

The TD-DFT-computed Abs spectrum for model $\mathbf{1}^{\mathbf{BS}}$ is dominated by a single feature in the visible region (Figure 7), which agrees well with our experimental results, as only one of the two Abs bands observed in this region is in fact attributable to **1** (Section 3.A).[53] However, the position and intensity of this feature are substantially overestimated by the TD-DFT method. To compensate for this deficiency, the TD-DFT-predicted

(53) Craft, J. L.; Horng, Y. C.; Ragsdale, S. W.; Brunold, T. C. *J. Biol. Inorg. Chem.* **2004**, *9*, 77–89.

Table 3. Excited-State Parameters Determined by Simultaneous Fitting of the 4 K Abs and 77 K rR Excitation Profile Data of **1** Using TD Heller Theory

parameter	state 1
E_{00} (cm^{-1})[a]	14,500
Δ_{474}	1.9
Δ_{269}	0.9

[a] E_{00} is the energy of the zero-phonon transition between the group state and excited state.

Abs spectrum was red-shifted by ~4,800 cm^{-1} and scaled by a factor of 1/6. While the tendency of TD-DFT to overestimate the energies of electronic transitions is well documented,[9] the discrepancy between the experimental and computed transition intensities most likely indicates that the DFT/B3LYP calculations overestimate the Ni−S bond covalency in **1**. Additionally, the difficulties in isolating **1** (vide supra) complicate an accurate determination of experimental ε values.

The electron density difference map (EDDM) shown in Figure 7 shows that the dominant Abs feature of **1** arises from a ligand-to-metal charge transfer excitation with the disulfido π^*_σ-based MO acting as the donor and the Ni z^2-based MO acting as the acceptor orbitals (Figure 6A and C, respectively). This assignment of the 15,500 cm^{-1} absorption band as a disulfido π^*_σ-to-Ni z^2 charge transfer transition is corroborated by our rR spectroscopic data, since both the ν_{S-S} and ν_{Ni-S} modes are significantly enhanced by laser excitation into this feature (Figure 2).

III.D. Excited-State Distortions. To estimate the distortions of the S−S and Ni−S bonds of **1** in the excited state associated with the dominant Abs feature (Figure 1), we employed time-dependent (TD) Heller theory to simultaneously fit the 4 K Abs and 77 K rR excitation profile data presented in Section III.A.[43,44] The experimental 4 K Abs spectrum of **1** was first fit with a single Gaussian band (Figure 8, top) to estimate the zero-phonon energy E_{00}. The dimensionless displacement parameters $|\Delta_{474}|$ and $|\Delta_{269}|$ associated with distortions of the S−S and Ni−S modes, respectively, were then systematically varied until the best simultaneous fit of the experimental Abs and rR profile data was achieved (Table 3, Figure 8).

The dimensionless displacement parameters, Δ_n, can be converted to the nuclear distortions along internal coordinates, Δr_i (Å), using eq 2.[54]

$$\Delta r_i = 5.8065 \cdot \sum_n L_{i,n} \cdot \frac{\Delta_n}{\sqrt{\nu_n}} \qquad (2)$$

Here, $L_{i,n}$ is the ith element of the mass-weighted eigenvector, $\mathbf{L}_n$, for the nth normal mode (as obtained from the NCA, Supporting Information, Table S3), and ν_n is the energy of the vibrational mode in cm^{-1}. The sign of Δ, which cannot be obtained from the TD Heller analysis, can be determined by considering the nature of the electronic transition associated with the 15,500 cm^{-1} Abs band. On the basis of the rR data and TD-DFT

(54) Zink, J. I.; Kim Shin, K.-S. Molecular Distortions in Excited Electronic States Determined From Electronic and Resonance Raman Spectroscopy. In *Advances in Photochemistry*; Volman, D. H., Hammond, G. S., Neckers, D. C., Eds.; Wiley: New York, 1991; Vol. *16*.

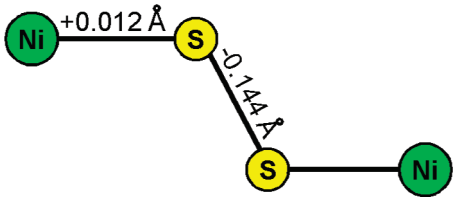

Figure 9. Experimentally derived nuclear distortions of **1** in the excited state associated with the dominant Abs feature in Figures 1 and 8.

computational results presented above, this transition is assigned as a disulfido → Ni charge transfer transition. The removal of electron density from the disulfido π^*_σ-based orbital (Figure 6A, HOMO-1) should cause a strengthening and, thus, shortening of the S−S bond, indicating that $\Delta_{474} < 0$. In contrast, population of the antibonding Ni-based LUMO lowers the Ni−S bond order and weakens this bond; hence, $\Delta_{269} > 0$. The predicted nuclear distortions obtained using this choice of signs for the Δ values are depicted in Figure 9. The magnitude and direction of the nuclear distortions obtained from our TD Heller analysis of **1** are consistent with those obtained for $[\{(TMPA)Cu\}_2(S_2)]^{2+}$, in which the disulfido bond was predicted to contract by 0.04 Å in the excited state corresponding to the disulfido π^*_σ-to-Cu z^2 charge transfer transition.

IV. Discussion

IV.A. Spectral and Electronic Properties of 1. To enhance our understanding of Ni−S bonding interactions, which play important structural and catalytic roles in several metalloenzymes, we have investigated the geometric and electronic structures of a synthetic dinickel(II) compound, **1**. The Abs spectrum of **1** is dominated by an intense disulfido-to-Ni charge transfer transition. Consistent with this assignment, the rR spectrum of **1** obtained upon laser excitation in resonance with this transition shows significant enhancement of the ν_{S-S} and ν_{Ni-S} vibrational features (Figure 2), and the rR excitation profiles of these vibrations closely mirror the 15,500 cm^{-1} Abs band (Figure 1).

Our MCD spectroscopic and DFT computational results indicate that **1** consists of two high-spin Ni^{II} monomers that are antiferromagnetically coupled to produce a diamagnetic ground state. As shown in Figure 6 and Table 2, the disulfido π^* and Ni 3d orbitals are in close energetic proximity, which results in significant mixing of Ni and disulfido orbital character in the frontier MOs. This mixing leads to highly covalent Ni−S σ-bonding interactions[55] and produces an efficient superexchange pathway for antiferromagnetic coupling (Figure 6A).

IV.B. Comparison of Nickel and Copper Disulfido Species. The M−S bonds are stronger in the dicopper(II) species $[\{(TMPA)Cu\}_2(S_2)]^{2+}$ than in **1**, based on NCAs of the vibrational data obtained for these species (Table 4).[11] This finding is in accordance with the trend observed for the analogous peroxo dimers.[10] The weaker bonds in the nickel species can be rationalized in terms of the different effective nuclear charges of Ni^{II} (Z_{eff} = 7.20) and Cu^{II} (Z_{eff} = 7.85).[10] Because of this difference, the energy gap between the metal 3d and disulfido π^* orbitals is smaller in the $Cu_2(S_2)$ species than in **1**, which results in stronger M−S bonding interactions in the copper dimer. Somewhat surprisingly, however, the Cu−S bonds in the copper dimer are only ∼0.19 mdyn/Å stronger than the Ni−S bonds in **1** (Table 4), possibly because of the relatively diffuse nature of the S 3p orbitals. As a result, the degree of π^*_σ-to-metal charge donation and, thus, the S−S bond strength are comparable in these dimers. Note that on the basis of previous work, the variation in the supporting ligand (tmc versus TMPA) and minor differences in the M−S−S bond angles should minimally affect the overall M−S and S−S bond strengths in these two species.[10]

Table 4. NCA-Derived Force Constants (in mdyn/Å) in Analogous Peroxo and Disulfido Species (M = Ni^{II}, Cu^{II}; L = O, S)

	O_2^{2-} [a]	S_2^{2-} [a]	H_2O_2 [a]	H_2S_2 [a]	$Ni_2(O_2)$ [b]	$Ni_2(S_2)$	$Cu_2(O_2)$ [a]	$Cu_2(S_2)$ [a]
k_{L-L}	2.76	1.88	3.84	2.77	2.58	2.40	3.11	2.41
k_{M-L}					1.52	2.69	2.02	2.88

[a] Ref 11. [b] Ref 10.

IV.C. Comparison of Peroxo and Disulfido Dimers. As revealed by the results of the NCAs (Table 4), the relative Ni−L and L−L bond strengths of **1** and **2** follow the trend observed in analogous *trans*-μ-1,2-L_2 $(Cu^{II})_2$ dimers (L = O, S). In the dinickel(II) complexes, the disulfido bond is weaker than the peroxide bond (k_{S-S} = 2.40 mdyn/Å and k_{O-O} = 2.58 mdyn/Å). A comparison of the bond strengths reported for H_2S_2 and H_2O_2 (Table 4) reveals that the S−S bond is intrinsically weaker than the O−O bond, by ∼28%.[11] The relative bond strengths of the disulfido and peroxo dinickel(II) species also correlate with the optimized S−S and O−O bond lengths of 2.097 and 1.436 Å for **2** and **1**, respectively.[10]

In contrast to the trend observed for the L−L bond strength, the Ni−L bond is weaker in **2** than in **1** (k_{Ni-O} = 1.52 mdyn/Å, k_{Ni-S} = 2.69 mdyn/Å). This result can be attributed to the higher energy and more diffuse nature of the sulfur 3p orbitals relative to the oxygen 2p orbitals, which results in greater mixing of the former with the Ni 3d orbitals and, thus, a larger k_{Ni-S} relative to k_{Ni-O}. The difference in relative valence orbital energies is also manifested by the fact that the dominant S → Ni charge transfer transition of **1**, observed at 15,500 cm^{-1}, occurs at considerably lower in energy than the analogous O → Ni charge transfer transition of **2**, which occurs at 21,900 cm^{-1}.

V. Summary and Conclusions

The results obtained in this combined spectroscopic and computational investigation of the dinickel(II) complex $[\{(tmc)Ni\}_2(S_2)]^{2+}$ (**1**) provide insight into the nature of the Ni−S bonding interactions in end-on $Ni_2(S_2)$ dimers and allow for a direct comparison to analogous *trans*-μ-1,2-L_2 $(M^{II})_2$ (M = Cu^{II}, Ni^{II}; L = O, S) species. As expected, the Ni−L bonding interactions in **1** are more covalent than in **2**, which is most evident from the stronger Ni−L bonds (k_{Ni-S} = 2.69 mdyn/Å versus k_{Ni-O} = 1.52 mdyn/Å) and the increased efficiency of the antiferromagnetic superexchange pathways in the disulfido system. Nonetheless, the M−S and S−S bonds are considerably weaker in **1** than in $[\{(TMPA)Cu\}_2(S_2)]^{2+}$ because of the decreased covalency of the Ni−S bonding interaction, which can be attributed to the lower effective nuclear charge of Ni^{II} compared to Cu^{II}.

(55) Fiedler, A. T.; Brunold, T. *Inorg. Chem.* **2007**, *46*, 8511–8523.

Consequently, the bridging $(S_2)^{2-}$ moiety of **1** is expected to be relatively electron-rich and thus primed for nucleophilic attack on electron-deficient substrates. Experimental studies aimed at exploring the reactivity of **1** are in progress.

Acknowledgment. We thank Professor Frank Neese, Universität Bonn, for providing us with a free copy of the ORCA software package. This work was supported by the NSF Graduate Research Fellowship program (K.M. V.H.) and by the NSF (CHE-0518508 and CHE-0809603 to C.G.R.).

Supporting Information Available: Atomic coordinates of the geometry-optimized model of **1** (Table S1), comparison of key structural parameters obtained from geometry optimizations of models of **1** featuring truncated and full molecular structures of the tmc ligand (Table S2), TD-DFT computed Abs spectra for the truncated and full models of **1** (Figure S1), parameters used for NCA of **1** (Table S3), rR excitation profiles of the ν_{Ni-N} vibrational modes (Figure S2), additional rR data (Figure S3), low-temperature Abs data (Figure S4), energies and compositions of all Ni d-based spin down MOs (Table S4). This material is available free of charge via the Internet at http://pubs.acs.org.